Nano Research
2021, 14(7): 2301–2308

ISSN 1998-0124 CN 11-5974/O4
https://doi.org/10.1007/s12274-020-3225-7

Research Article

Free-standing hybrid films comprising of ultra-dispersed titania nanocrystals and hierarchical conductive network for excellent high rate performance of lithium storage

Kunlei Zhu[1,2] (✉), Chenyu Li[2], Yushuang Jiao[1], Jiawen Zhu[1], Hongtao Ren[3], Yufeng Luo[4], Shoushan Fan[4], and Kai Liu[2] (✉)

[1] College of Chemistry and Chemical Engineering, Qufu Normal University, Jingxuan West Road NO.57, Qufu 273165, China
[2] State Key Laboratory of New Ceramics and Fine Processing, and Key Laboratory of Advanced Materials of Ministry of Education, School of Materials Science and Engineering, Tsinghua University, Beijing 100084, China
[3] School of Materials Science and Engineering, Liaocheng University, Hunan Road No. 1, Liaocheng 252000, China
[4] Department of Physics and Tsinghua-Foxconn Nanotechnology Research Center, Tsinghua University, Beijing 100084, China

Received: 17 September 2020 / **Revised:** 28 October 2020 / **Accepted:** 5 November 2020

ABSTRACT

The construction of advanced electrode materials is key to the field of energy storage. Herein, a free-standing anatase titania (TiO_2) nanocrystal/carbon nanotube (CNT) film is reported using a simple and scalable sol-gel method, followed by calcination. This unique free-standing film comprises ultra-small TiO_2 nanocrystals (~ 5.9 nm) and super-aligned CNTs, with ultra-dispersed TiO_2 nanocrystals on the surfaces of the CNTs. On the one hand, these TiO_2 nanocrystals can significantly decrease the diffusion distance of the charges and on the other hand, the cross-linked CNTs can act as a three-dimensional (3D) conductive network, allowing the fast transport of electrons. In addition, the film is free-standing, without requiring electrode fabrication and additional conductive agents and binders. Owing to these above synergistic effects, the film is directly used as an anode in Li-ion batteries, and delivers a high discharge capacity of ~ 105 $mAh{\cdot}g^{-1}$ at high rate of 60 C (1 C = 170 $mA{\cdot}g^{-1}$) and excellent cycling performance over 2,500 cycles at 30 C. These results indicate that the free-standing anatase TiO_2 nanocrystal/CNT film affords a superior performance among the various TiO_2 materials and can be a promising anode material for fast-charging Li-ion batteries. Moreover, the TiO_2/CNT film exhibits an areal capacity of up to 2.4 $mAh{\cdot}cm^{-2}$, confirming the possibility of its practical use.

KEYWORDS

carbon nanotubes, free-standing, high rate, Li-ion batteries, TiO_2, ultra-small

1 Introduction

With an increase in population and subsequent environmental deterioration, it is important to develop "green and clean" vehicles. Electric vehicles recognized by the international agencies can meet these requirements, which has led to a sharp increase in the global demand of these vehicles in recent years [1, 2]. Currently, Li-ion batteries with high energy densities and excellent cycling lives are considered as one of the most promising storage devices to use in the commercially available electric vehicles. However, these electric vehicles are still restricted by a limited driving-range. There are two methods to address this issue. One is to further increase the energy densities of the Li-ion batteries by using electrode materials with high specific capacities. For example, Li-ion batteries with high energy densities (> 300 $Wh{\cdot}Kg^{-1}$) can be obtained using Li $[Ni_xCo_yMn_z]O_2$ (NMC, $x + y + z = 1$) layered oxides as the cathode [3, 4] and Si-based material as anodes [5–7]. The specific capacities of the NMC-type materials increase with an increase in the Ni content, while its thermal instability decreases [3]. This can probably lead to the decomposition of the cathode materials and release of oxygen caused by the thermal effects during repeated charge–discharge cycles, resulting in serious safety problems. Moreover, Si-based anode materials suffer from a large volume change of ~ 300% during the lithiation/delithiation processes, which causes the pulverization of the electrode and continuous electrolyte consumption due to the repeated formation of solid electrolyte interphase [7], resulting in a sharp capacity decay of the Li-ion batteries. An additional method involves the development of novel materials with fast-charging capacities. The fast-charging capacity of the Li-ion battery is mainly determined by the anode materials. However, the capacities of the traditional anode materials (e.g., graphite) decrease sharply when batteries have high current densities under fast-charging conditions. Therefore, it is necessary to develop novel anode materials to achieve fast charging of the Li-ion batteries with excellent high rate performance.

TiO_2 is one of the most promising anode materials for Li-ion batteries. On the one hand, TiO_2 shows a small lattice change (< 4%) during lithium insertion/extraction and can be used at a high operating voltage of 1–3 V (vs. Li^+/Li), affording a high rate performance without the collapse of the structure, and good safety by suppressing the formation of solid electrolyte

Address correspondence to Kunlei Zhu, zhukunlei_123@163.com; Kai Liu, liuk@tsinghua.edu.cn

interface (SEI) layers and lithium dendrites [8, 9]. On the other hand, TiO_2 has advantages including low cost, availability, and environmental friendliness, which can allow the large-scale manufacture of TiO_2 anodes for Li-ion batteries. Thus, TiO_2 has attracted increasing attention as a promising material for Li-ion batteries [10–23]. The electrochemical performance of TiO_2, particularly the high rate capacity, is determined by the chemical diffusivity of Li in TiO_2, which mainly depends on two factors: electronic conductivity of TiO_2 electrodes and diffusivity of Li ions in TiO_2 [24]. To increase the electronic conductivities of TiO_2 electrodes, the composites are typically fabricated by incorporating conductive components such as graphene [9, 10, 13–15, 22], graphitic carbon [16], activated carbon fabric [25], and carbon nanotubes (CNTs) [26]. To increase the diffusivity of Li ions in TiO_2, nanostructure engineering is an effective strategy to decrease the diffuse distance of Li ions by designing mesoporous TiO_2 with a porous structure [8, 19, 24, 27], TiO_2 nanoparticles/nanocrystals [13–15, 17], and hollow nanostructures [16, 18, 21, 28]. In addition, non-conductive binders are added to combine the active materials and conductive agents in traditional electrodes, which can result in poor contact of these electrode materials with the substrates and decreased electron transport. Free-standing films, which are the representatives of advanced electrodes without binders [29, 30], provide clean interfaces between the active materials and conductive agents. However, the construction of free-standing electrodes that not only have ultrasmall nanocrystals with ideal dispersity and good crystallinity, but also contain hierarchical conductive networks to achieve satisfactory specific capacities and high rate performances still remains challenging.

Herein, the fabrication of a free-standing anatase TiO_2 nanocrystal/CNT hybrid film is reported, where TiO_2 nanocrystals with ultrasmall sizes (~ 5.9 nm) and good dispersion act as lithium insertion hosts with a significantly decreased diffusion distance. The CNTs framework plays a key role as a three-dimensional (3D) network in enhancing the electronic conductivity of the electrode. The hybrid film exhibits an impressive discharge capacity of up to ~ 105 $mAh \cdot g^{-1}$ at high rate of 60 C and stable cycling performance with a capacity > 100 $mAh \cdot g^{-1}$, which is reserved even after 2,500 cycles at 30 C. These findings prove that the hybrid film can be a potential candidate for fast-charging anode materials for Li-ion batteries. Furthermore, the anatase free-standing TiO_2/CNT film affords an areal capacity of up to 2.4 $mAh \cdot cm^{-2}$, suggesting its potential application in industrial manufacturing.

2 Experimental

2.1 Materials

Tetrabutyl titanate (TBT, ≥ 99.7%) and concentrated ammonia water (28%–30%) were purchased from Sigma-Aldrich (St. Louis, Missouri, USA). Anhydrous ethanol (≥ 99.5%) and commercially available nanoparticles (~ 25 nm) were purchased from Aladdin Biochemical Technology Co., Ltd. (Shanghai, China). Super-aligned CNT arrays with diameters of 20–30 nm were prepared on silicon wafers using a low-pressure chemical vapor deposition system, where iron was used as the catalyst and acetylene as the precursor [31, 32].

2.2 Methods

Free-standing amorphous TiO_2/CNT films were first fabricated using a facile *in-situ* sol-gel method [29], where super-aligned CNT arrays (40 mg) were scraped off the silicon wafer and dispersed in 200 mL of ethanol using an ultrasonication probe (SCIENTZ-950E, SCIENTZ Biotechnology Co., Ltd., Ningbo, China) for one hour to form a CNT dispersion solution. Then, concentrated ammonia water (0.6 mL) was added to the above CNT dispersion solution. After stirring for 10 min at 25 °C, TBT (2 mL) was added dropwise to the dispersion solution, and the reaction mixture was continuously stirred for eight hours at 25 °C. Next, the dispersion mixture was filtered by vacuum filtration and dried in air at room temperature, and continuous amorphous TiO_2/CNT films were formed on the filter paper. The weight ratio of TiO_2 can be controlled by adjusting the amount of concentrated ammonia water (Fig. S1 in the Electronic Supplementary Material (ESM) [29]. Finally, free-standing anatase TiO_2 nanocrystal/CNT films were obtained after the amorphous TiO_2/CNT films were thermally treated at 400 °C for two hours in Ar. Amorphous and anatase TiO_2 nanoparticles were prepared using the similar synthetic process without the addition of CNTs, and were collected by centrifugation.

An improved sol-gel method was used to prepare the free-standing anatase TiO_2/CNT films with a high weight ratio of TiO_2. In a typical synthesis, the super-aligned CNT arrays (80 mg) were scraped off the silicon wafer and dispersed in 200 mL of ethanol. Then, TBT (2 mL) was added dropwise to the dispersion solution at 25 °C with continuous stirring. The mixture dispersion solution was kept static at room temperature in a fume hood until ethanol was completely evaporated. Thereafter, free-standing amorphous TiO_2/CNT films were obtained after TBT was slowly and continuously hydrolyzed with water in air. Finally, anatase TiO_2/CNT films with a high weight ratio of TiO_2 were obtained after the amorphous TiO_2/CNT films were thermally treated at 500 °C for two hours in Ar.

2.3 Characterization and measurement

Scanning electron microscopy (SEM) images were obtained using an FEI Sirion 200 microscope (5 kV, FEI Company, Hillsboro, Oregon, USA). Transmission electron microscopy (TEM) images, high-angle annular dark-field scanning transmission electron microscopy (HAADF-STEM), and energy dispersive X-ray (EDX) elemental mapping images were obtained using an FEI Tecnai G2F20 microscope (200 kV, FEI Company). X-ray diffraction (XRD) patterns were collected by employing a Rigaku D/max 2500 PC diffractometer (40 kV, 40 mA, Rigaku Corporation, Tokyo, Japan). Raman spectra were obtained using an integrated laser Raman system (LABRAMHR, Jobin Yvon, Horiba, Ltd., Kyoto, Japan) with an argon laser (514.5 nm) as the excitation source. Thermogravimetric (TGA) experiments were performed using a Netzsch STA449C instrument (Erich NeTZSCH GmbH & Co. Holding KG, Selb, Germany) from 25 to 800 °C under air at a heating rate of 10 $°C \cdot min^{-1}$.

Coin-type cells (2016 size) were assembled in a glove box filled with high-purity Ar and the concentrations of water and oxygen were below 0.1 ppm. The TiO_2 mass loading of TiO_2/CNT films for each electrode was ~ 1.2 $mg \cdot cm^{-2}$. Anatase TiO_2 nanocrystal/CNT films were cut into disks with a diameter of 8 mm using a laser and directly used as the working electrodes. The anatase TiO_2/CNT film with 85 wt.% TiO_2 underwent the same cell assembly process, except that the TiO_2 mass loading for each electrode was ~15 $mg \cdot cm^{-2}$. The specific capacities and areal capacities of the TiO_2/CNT films were calculated based on the mass of TiO_2 or TiO_2/CNTs and the areas of the electrodes, respectively. The pristine TiO_2 was processed into the electrodes by mixing TiO_2 nanoparticles and polytetrafluoroethylene at 80:10 weight ratio. Commercially available 25-nm TiO_2 nanoparticles were processed into the electrodes using a traditional method [11].

The slurry was prepared by mixing TiO_2 nanoparticles, acetylene black, and polyvinylidene fluoride at 70:20:10 weight ratio. The slurry of the mixture was cast on alumina foil using doctor blade technology, and each electrode with a diameter of 14 mm constituted 1–1.5 mg·cm^{-2} of TiO_2. Pure lithium foils were used as both the counter and reference electrodes. A porous polymer film (Celgard 2400, Celgard LLC, Charlotte, North Carolina, USA) was used as the separator. The electrolyte was a solution of 1 M $LiPF_6$ dissolved in a mixture of ethylene carbonate, diethyl carbonate and dimethyl carbonate and was provided by Tianjin Jiuniu Power Sources Material Co., Ltd. (Tianjin, China). Galvanostatic charge–discharge tests were performed in the voltage range of 1.0–3.0 V using a LAND CT2001A battery test system (Wuhan Land Electronic Co. Ltd., Wuhan, China). Electrochemical impedance spectroscopy (EIS) mesurements were performed by employing an electrochemical analyzer (CHI 760E, China) with a perturbation of 5 mV under open-circuit voltage conditions. All electrochemical tests were performed at room temperature.

3 Results and discussion

Figure 1 shows the synthetic process of the free-standing anatase TiO_2 nanocrystal/CNT film. Super-aligned CNT arrays that were used as 3D supports, were prepared on silicon wafers via chemical vapor deposition [31]. The CNTs with diameters of 20–30 nm had a clean surface (Fig. S2 in the ESM), with strong van der Waals interactions, resulting in facile formation of free-standing 3D porous films by ultrasonication, followed by vacuum filtration [29] or drying [33]. First, the CNTs were scraped off the silicon wafer and dispersed in ethanol (containing the desired amount of concentrated ammonia water) by ultrasonication to form a CNT dispersion solution (step 1 in Fig. 1). Then, TBT was added dropwise into the above solution with continuous stirring. As a result, the amorphous TiO_2 nanoparticles were anchored on the surfaces of the CNTs after the hydrolysis and condensation of TBT (step 2 in Fig. 1) via a sol-gel process, leading to the formation of an amorphous TiO_2/CNT composite. Next, the above dispersion mixture was filtered by vacuum filtration and dried in air at room temperature, and the free-standing amorphous TiO_2/CNT films were formed on the filter paper (Fig. 1(d)). Finally, free-standing anatase TiO_2 nanocrystal/CNT films were obtained (Fig. 1(e)) after the amorphous TiO_2/CNT films were subjected to calcination (step 3 in Fig. 1). Free-standing anatase TiO_2 nanocrystal/CNT films are easily processable and can be cut into the desired shapes (e.g., disks shown in Fig. 1(f)) using a laser. Thus, free-standing anatase TiO_2 nanocrystal/CNT disks can be directly used as anodes for Li-ion batteries without requiring an electrode preparation process, and additional conductive agents and binders are not required, demonstrating the efficient and simple preparation of the free-standing films.

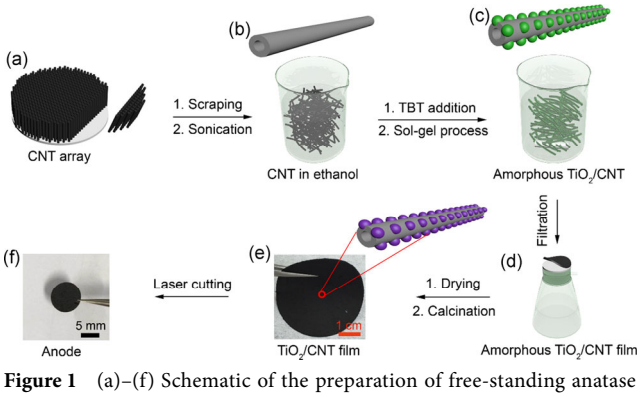

Figure 1 (a)–(f) Schematic of the preparation of free-standing anatase TiO_2 nanocrystal/CNT film.

Figure 2 shows the SEM images of the prepared films. For amorphous TiO_2/CNT films, CNTs interweave with each other, forming a 3D structure (Figs. 2(a) and 2(b) and inset), whereas TiO_2 nanoparticles are invisible because of their very small sizes. In addition, no bulk TiO_2 is deposited on the surfaces of the CNTs (Fig. 2(b)), indicating no formation of bulk TiO_2 or aggregates with the hydrolysis and condensation of TBT; TiO_2 nanoparticles are also well-dispersed on the CNT surfaces. After selective calcination at 400 °C for two hours in Ar, the morphology of anatase TiO_2 nanocrystal/CNTs shows no noticeable changes compared to that of the amorphous TiO_2/CNT films (Figs. 2(c) and 2(d)), suggesting that the film is stable. TiO_2 nanocrystals can be found on the surfaces of the CNTs in a magnified SEM image (inset in Fig. 2(d)). The weight ratio of TiO_2 in the TiO_2 nanocrystal/CNT film is 24.1 wt.%, based on the TGA measurements (Fig. S3 in the ESM).

To observe the local microstructures of these films, TEM studies were performed (Fig. 3). In sharp contrast to the pristine CNTs with smooth surfaces (Fig. S2 in the ESM), TiO_2 nanoparticles are uniformly deposited on the surfaces of the CNTs (Fig. 3(a)) in the amorphous TiO_2/CNT films owing to the effective chemical coupling between TiO_2 and CNTs through strong interaction between the CNTs and Ti with unfilled 3d orbitals [34]. Magnified TEM images show that these amorphous TiO_2 nanoparticles are very small in size, i.e., 3–10 nm (Fig. 3(b)). The high-resolution TEM (Fig. S4 in the ESM) reveals the disordered structure of the amorphous TiO_2/CNT film. After calcination, these nanoparticles crystallize into spherical TiO_2 nanocrystals, which are still uniformly deposited on the surfaces of the CNTs without noticeable aggregation (Fig. 3(d) and Fig. S5 in the ESM). To determine the sizes of the TiO_2 nanocrystals, greater than 1,000 nanocrystals anchored on the CNTs were collected (Fig. S5 in the ESM). As shown in Fig. 3(c), the sizes of the TiO_2 nanocrystals are in the 2–15 nm range, and the mean size is estimated to be only ~ 5.9 nm, indicating the fast transport of Li^+ within the TiO_2 nanocrystals due to the significantly decreased transport distance. The magnified TEM image further reveals that these TiO_2 nanocrystals are isolated and tightly adhere to the CNTs during growth (Fig. 3(e)), indicating the maximization of the Li storage sites of the TiO_2 nanocrystals and contact interface between the TiO_2 nanocrystals and electrolyte, as well as rapid electron transfer between the TiO_2 nanocrystals and CNTs. The high-resolution TEM image (Fig. 3(f)) shows lattice plane spacings of 0.19 nm and 0.34 nm, which are indexed to the (200) plane of anatase

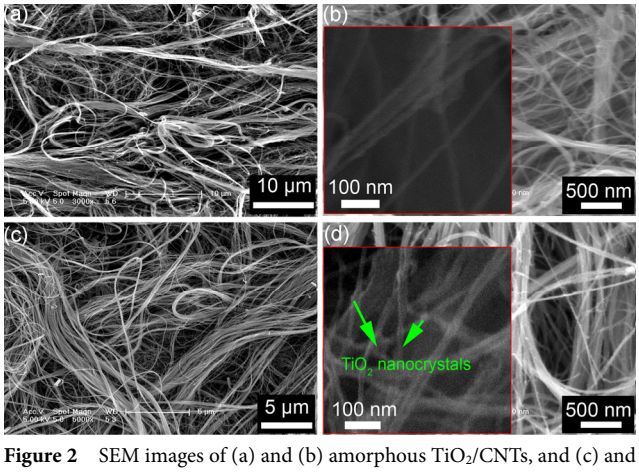

Figure 2 SEM images of (a) and (b) amorphous TiO_2/CNTs, and (c) and (d) anatase TiO_2 nanocrystal/CNTs. Inset: Magnified SEM images.

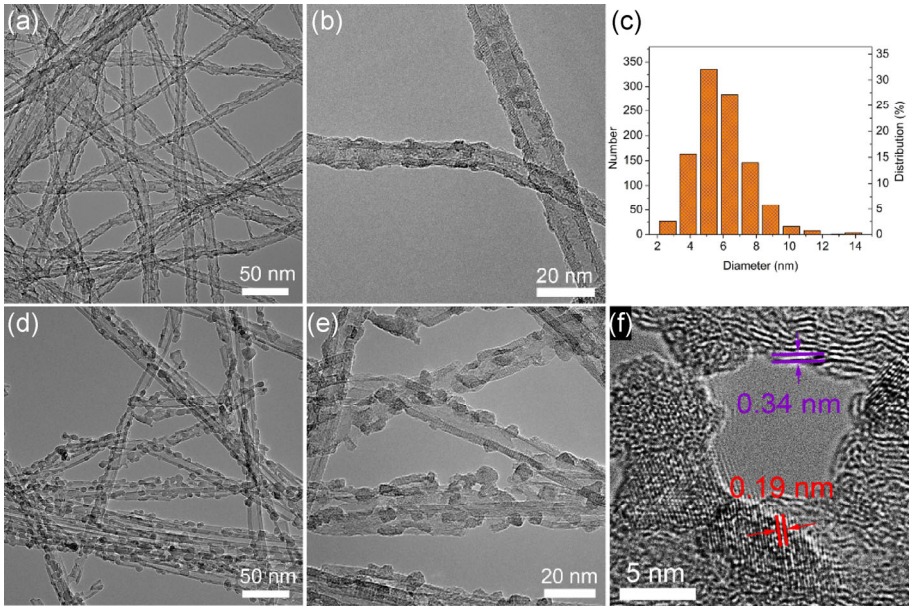

Figure 3 TEM images of (a) and (b) amorphous TiO_2/CNTs, and (d)–(f) anatase TiO_2 nanocrystal/CNTs. (c) Size distribution of the anatase TiO_2 nanocrystals coated on the CNTs.

TiO_2 and (002) plane of graphitic carbon, respectively [35, 36], suggesting the existence of anatase TiO_2 and CNTs.

Moreover, HAADF-STEM data and EDX elemental mapping images were collected to determine the distribution of TiO_2 nanocrystals (Fig. S6 in the ESM). Ti and O are uniformly dispersed on the surface of the CNT bundle, as shown in Figs. S6(c) and S6(d) in the ESM. Therefore, it is unambiguously confirmed that TiO_2 nanocrystals are uniformly coated on the CNTs surfaces, in agreement with the TEM results (Fig. 3(d)) and Fig. S5 in the ESM).

Pristine TiO_2 sample prepared without addition of the CNTs and calcination shows a wide peak at ~ 20°–37° in the XRD pattern (orange line in Fig. 4(a)), indicating that it has an amorphous structure. The amorphous characteristics of the TiO_2/CNT film is also confirmed by the XRD pattern, where do not show peaks of crystallographic TiO_2 (blue line in Fig. 4(a)). In addition, two peaks at 2θ values of = 25.8° and 43° are indexed to the (002) and (100) reflections of the CNTs in the amorphous TiO_2/CNT film. In the XRD pattern of anatase TiO_2 nanocrystal/CNT film (red line in Fig. 4(a)), the peaks at 2θ values of 25.3°, 37.8°, 48.0°, 53.9°, and 55.1° are observed, which are indexed to the (101), (004), (200), (105), and (211) planes of anatase TiO_2 [14–19], respectively, confirming the anatase crystal structure (JCPDS card no. 21-1272; space group $I4_1/amd$; $a_0 = b_0 = 3.7852$ Å, $c_0 = 9.5139$ Å) of the TiO_2 nanocrystals. In addition, a shoulder peak is observed at 2θ value of = 25.8°, which is attributed to the (002) reflections of CNTs.

Raman spectra for the three films were also recorded, and the results are shown in Fig. 4(b). The amorphous TiO_2/CNT film exhibits Raman signals similar to those of the CNT film, with the absence of TiO_2 signal because of the amorphic characteristics of TiO_2. In addition, the Raman signals at 1,350 and 1,580 cm^{-1} can be attributed to the D and G peaks, respectively, of the CNTs [37]. The TiO_2 nanocrystal/CNT film exhibits Raman signals at 153, 202, 394, 207, 512, and 631 cm^{-1}, corresponding to the anatase Raman active modes of $E_{g(1)}$, $E_{g(2)}$, $B_{1g(1)}$, A_{1g}, $B_{1g(2)}$ and $E_{g(3)}$, respectively [38]. This further confirms the anatase crystal phase of the TiO_2 nanocrystals, which is consistent with the TEM and XRD results.

The free-standing anatase TiO_2 nanocrystal/CNT film was investigated as an anode for the Li-ion batteries and was assembled into 2016-size coin half-cells. A tedious electrode preparation must typically be performed before the cell assembly for power-type materials, while the free-standing film described in this study can be directly used as a working electrode after cutting it into disks using a laser (digital photograph shown in Fig. 1), where no additional conductive agents and binders are needed. As shown in Fig. 5(a), the discharge–charge curve of the amorphous TiO_2/CNT film shows an unnoticeable voltage plateau, which is derived from the pseudocapacitive mechanism discussed in our previous report [29, 39]. For anatase TiO_2,

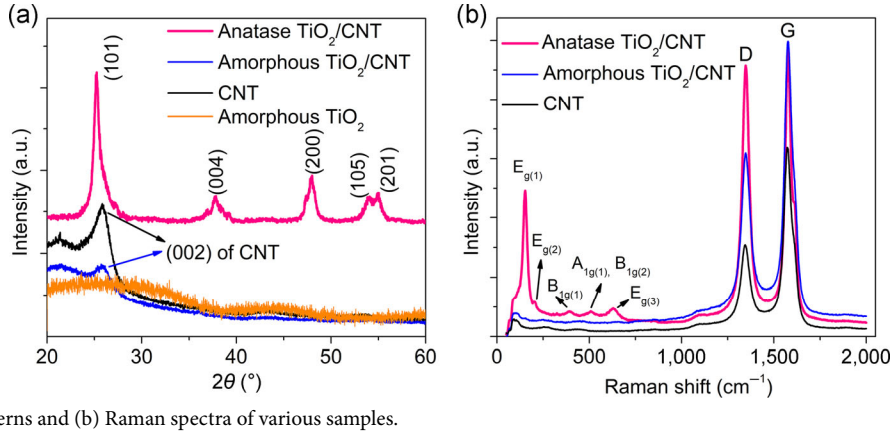

Figure 4 (a) XRD patterns and (b) Raman spectra of various samples.

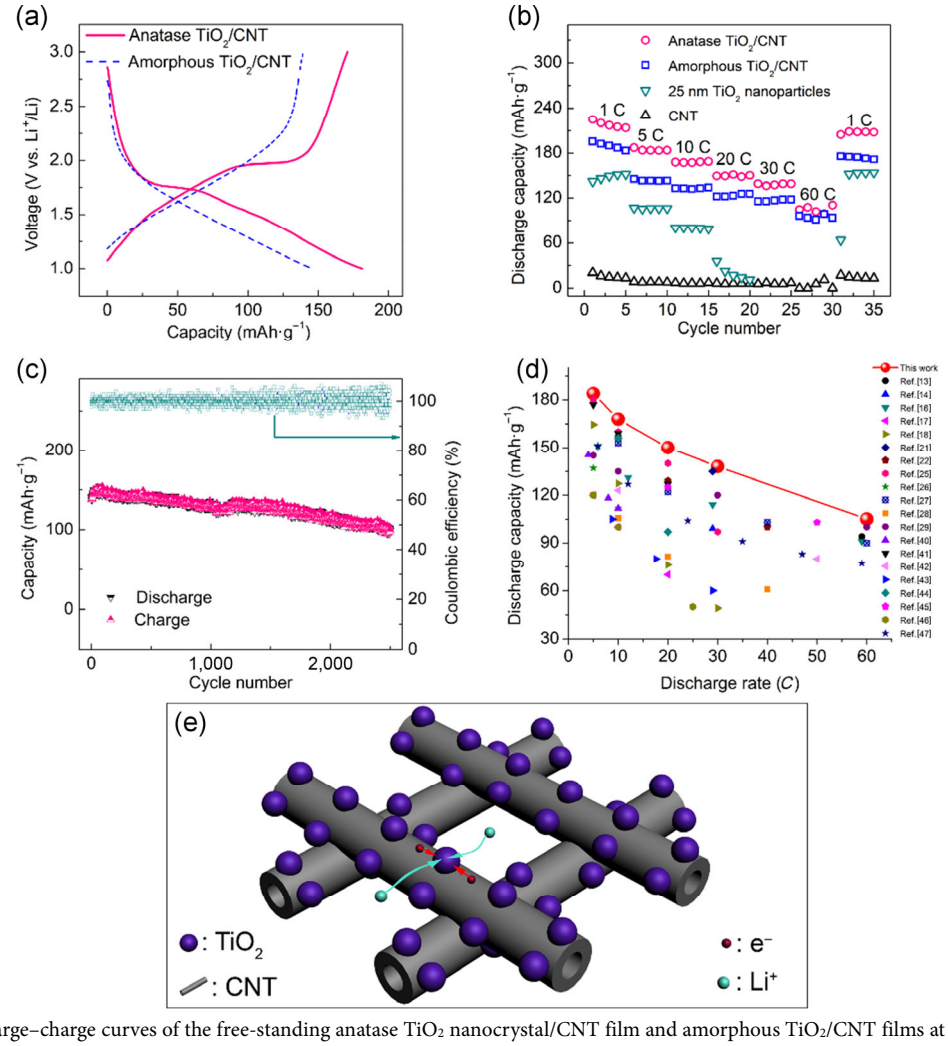

Figure 5 (a) Discharge–charge curves of the free-standing anatase TiO_2 nanocrystal/CNT film and amorphous TiO_2/CNT films at 5 C. (b) Rate capacity curves of the free-standing anatase TiO_2 nanocrystal/CNT film, amorphous TiO_2/CNT film, CNT film, and commercially available 25-nm nanoparticles. (c) Cycling performance of the free-standing anatase TiO_2 nanocrystal/CNT film at 30 C over 2,500 cycles. (d) Comparison of the high rate capacities of various TiO_2 materials at the current rates of 4–60 C. (e) Diagram showing the transport of electrons and Li ions within TiO_2 nanocrystal/CNT electrodes.

the electrochemical Li storage process can be expressed by the following half-cell equation [17, 21]

$$TiO_2 + x\,Li + x\,e^- \leftrightarrow Li_xTiO_2 \quad (0 < x \leq 1)$$

The Li storage process is expressed in the form of the discharge curve of anatase TiO_2 and can be divided into three stages [13, 14, 16, 17, 21]. The first stage is the formation of a solid solution domain of tetragonal anatase ($I4_1/amd$) and Li-poor tetragonal Li_xTiO_2 ($I4_1/amd$) after the intercalation of a small fraction of Li into TiO_2, with a sharp decrease in voltage from the open circuit voltage to ~ 1.7 V. For the free-standing anatase TiO_2 nanocrystal/CNT film, ~ 0.07 Li per TiO_2 unit is intercalated into anatase TiO_2, leading to the formation of $Li_{0.07}TiO_2$ ($I4_1/amd$). The second stage involves a phase change from Li-poor tetragonal Li_xTiO_2 ($I4_1/amd$) to Li-rich orthorhombic $Li_{0.55}TiO_2$ ($Imma$), with a voltage plateaus zone at ~ 1.7 V due to the coexistence of the Li-poor and Li-rich phases. The free-standing anatase TiO_2 nanocrystal/CNT film shows a noticeable discharge voltage plateau at ~ 1.75 V (Fig. 5(a)), in contrast to the amorphous TiO_2/CNT film, which shows no voltage plateau and unstable voltage output. The last stage can involve further lithium insertion into the surface/interface of TiO_2 showing a pseudocapacitive behavior [11, 13, 17]. Overall, after the discharge process, the free-standing anatase TiO_2 nanocrystal/CNT film affords a discharge capacity of 181 mAh·g^{-1}, which is significantly higher than that (146 mAh·g^{-1}) of the amorphous TiO_2/CNT film. Notably, charging is an inverse of the discharge process.

The rate capacities of various materials were then evaluated by discharging–charging at various current densities in the voltage range of 1.0–3.0 V (Fig. 5(b)). The pristine CNT film shows negligible discharge capacities at various current densities. For comparison, the commercially available 25-nm TiO_2 nanoparticles were processed into electrodes using a traditional method [13, 14], where acetylene black and polyvinylidene fluoride were used as the conductive agent and binder, respectively. These TiO_2 nanoparticles show discharge capacities of ~ 150, ~ 105, and ~ 80 mAh·g^{-1} at current rates of 1, 5, and 10 C, respectively, and the capacities approach 0 mAh·g^{-1} when current rates exceed 20 C. The amorphous TiO_2/CNT film exhibits discharge capacities of ~ 190, ~ 145, ~ 135, ~ 125, ~ 120, and ~ 100 mAh·g^{-1} at the current rates of 1, 5, 10, 20, 30, and 60 C, respectively. In contrast, the free-standing anatase TiO_2 nanocrystal/CNT film affords increased discharge capacities of ~ 218, ~ 184, ~ 168, ~ 150, ~ 138, and ~ 105 mAh·g^{-1} at current rates of 1, 5, 10, 20, 30, and 60 C, respectively. Moreover, the capacities can recover to ~ 208 mAh·g^{-1} when the current rate returns to 1 C. Moreover, the capacity of the anatase TiO_2 nanocrystal/CNT film exhibits a negligible drop after the removal of the capacity from CNT contribution (Fig. S7 in the ESM). In addition, the Coulombic efficiencies of the free-standing anatase TiO_2 nanocrystal/CNT film increase

distinctly at various current densities, compared to those of the amorphous TiO_2/CNT film (Fig. S8 in the ESM). The superior rate capacity of the anatase TiO_2/CNT film may be derived from the Li insertion into anatase TiO_2 nanocrystals, compared to that of the amorphous TiO_2/CNT film which has a disorder structure prohibits the Li^+ ions diffusion in these amorphous TiO_2 nanoparticles (Fig. S9 in the ESM). As indicated by the EIS data (Fig. S10 and Table S1 in the ESM), the anatase TiO_2 nanocrystal/CNT film has much decreased charge transfer resistance (R_{ct}) compared to that of the pristine TiO_2, highlighting the importance of CNT for electron transport. However, the R_{ct} of amorphous TiO_2/CNT film sharply increases with increasing cycles.

Furthermore, the free-standing anatase TiO_2 nanocrystal/CNT film exhibits excellent cycling performance (Fig. 5(c)). After 2,500 cycles at 30 C, the film still affords a discharge capacity of up to 100 mAh·g^{-1}, with a Coulombic efficiency of ~ 100% for each cycle. However, TEM image reveals that the TiO_2 nanocrystals tend to agglomerate together and change into sheet-like structure after cycling test (Fig. S11 in the ESM).

To highlight the excellent electrochemical performance of the free-standing anatase TiO_2 nanocrystal/CNT film, it was compared with those of various recently reported TiO_2 materials (Fig. 5(d)). The free-standing anatase TiO_2 nanocrystal/CNT film fabricated in this work affords remarkably improved high-rate capacities compared to those of various TiO_2-based materials [13, 14, 16–18, 21, 22, 25–29, 40–47] such as TiO_2 nanocrystal/reduced graphene oxide sheets [13], cTiO_2 hollow spheres [17], and TiO_2@C aerogel [41].

The excellent high rate electrochemical performance of this free-standing anatase TiO_2 nanocrystal/CNT film can be ascribed to the increased transport of Li ions and electrons (Fig. 5(e)), originating from the synergistic coupling effects of TiO_2 nanocrystals and CNTs. 1) The ultrasmall TiO_2 nanocrystals with sizes of only ~ 5.9 nm and good crystallinity not only provide abundant active sites for Li intercalation and maximize the contact interface with the electrolyte, but also decrease the diffusion path of Li ions because of the quantum size effect [48, 49]. 2) These CNTs interweave together, forming a 3D conductive channel, and provide a transport path for the electrons, resulting in the fast transport of electrons along the 3D support within the entire electrode. 3) Without use of a non-conductive binder, the interfaces of the TiO_2 nanocrystals and CNTs are clean, allowing electrons to rapidly cross these interfaces. In addition, a clean interface between this free-standing TiO_2 nanocrystal/CNT film and the collector is obtained, which also allows the fast transfer of electrons. Thus, owing to the synergistic coupling effects of TiO_2 nanocrystals and CNTs, the free-standing TiO_2 nanocrystal/CNT film permits the rapid transport of both Li ions and electrons within the complete electrode, leading to a fast charging–discharging without affecting the capacities.

TiO_2 is one of the most promising anode materials of the Li-ion batteries [50–53], it is necessary to check the possibility of its practical application. Thus, a free-standing anatase TiO_2/CNT film with a high TiO_2 content of up to 85 wt.% was prepared to determine the possibility of its practical application. To obtain a high weight ratio of TiO_2, an improved sol-gel method was employed to fabricate TiO_2/CNT films via the slow and continuous hydrolysis of TBT with water in air, followed by calcination. As observed in the TEM images (Figs. 6(a) and 6(b)), these CNTs are almost completely coated by TiO_2 owing to the deposition of a large amount of TiO_2. The film is still free-standing and directly used as an anode for Li-ion batteries, with the TiO_2 mass loading of up to 15 mg·cm^{-2}. After the discharge process is completed at 0.51 mA·cm^{-2} (Fig. 6(c)), the areal capacity of the TiO_2/CNT film is up to 2.4 mAh·cm^{-2}, which is within the range of typical areal capacities of the commercial Li-ion batteries [54]. The free-standing anatase TiO_2/CNT film exhibits a typical discharge voltage plateau at ~ 1.7 V (Fig. 6(c)) and is expected to afford a stable voltage output compared to that of the amorphous TiO_2/CNT film without a voltage plateau [29]. The areal capacity of the TiO_2/CNT films is ~ 2 mAh·cm^{-2} in the following charging process, leading to a Coulombic efficiency of 81.0% which is significantly higher than that of the amorphous TiO_2/CNT film (< 60%) [29]. The Coulombic efficiency increases up to 92.8% and 97.7%, respectively, for the 2nd and 5th cycle (Fig. 6(c)).

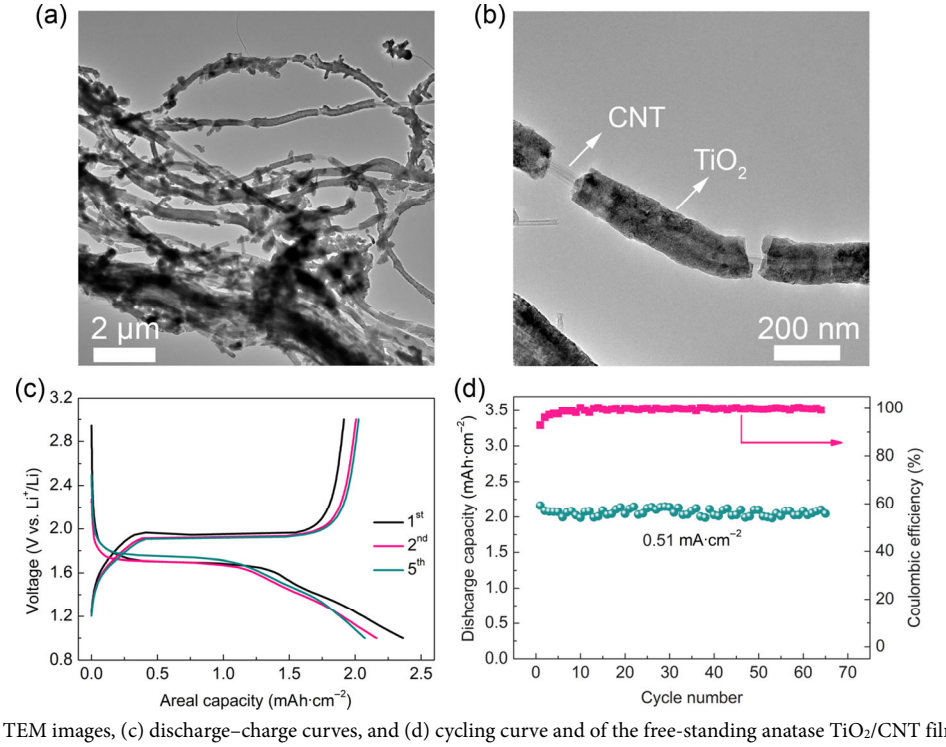

Figure 6 (a) and (b) TEM images, (c) discharge–charge curves, and (d) cycling curve and of the free-standing anatase TiO_2/CNT film with 85 wt.% TiO_2.

Moreover, the free-standing anatase TiO_2/CNT film affords a stable discharge capacity of ~ 2 mAh·cm^{-2} (~ 120 mAh·g^{-1} based on the total mass of the TiO_2/CNT film) at 0.51 mA·cm^{-2} (0.2 C) over 70 cycles without capacity decay (Fig. 6(d) and Fig. S12 in the ESM), demonstrating the possibility of its practical application.

4 Conclusions

In summary, a unique free-standing anatase TiO_2 nanocrystal/CNT film is prepared using a simple and scalable sol-gel method, followed by calcination, where the anatase TiO_2 nanocrystals have ultrasmall sizes of only ~ 5.9 nm and are well-dispersed on the CNT surfaces. These CNTs are interweaved together and act as a 3D conductive network and robust support. The findings reveal that the rational design and modification can afford highly dispersed TiO_2 nanocrystals without aggregation on the CNT surfaces owing to the strong chemical coupling/interactions between TiO_2 and CNTs. Furthermore, the film can be directly used as an anode in Li-ion batteries, affording a high specific discharge capacity of ~ 105 mAh·g^{-1} at 60 C, high rate capacity, and good cycling performance over 2,500 cycles at 30 C, without requiring electrode fabrication and the addition of conductive agents and binders. These results indicate that the free-standing anatase TiO_2 nanocrystal/CNT film can be a promising anode for fast-charging Li-ion batteries. Moreover, with TiO_2 content of up to 85 wt.%, the free-standing anatase TiO_2/CNT film exhibits an areal capacity of up to 2.4 mAh·cm^{-2}, suggesting its practical application in industrial manufacturing.

Acknowledgements

The authors acknowledge the financial support from the National Key R&D Program of China (No. 2018YFA0208401), Basic Science Center Project of NSFC under grant No. 51788104, Scientific Research Foundation of Qufu Normal University (No. 613701), and Fund of Key Laboratory of Advanced Materials of Ministry of Education (No. 2020AML04). We thank Dr. Bolun Wang for his kind help in revising the manuscript.

Electronic Supplementary Material: Supplementary material (TGA curve, TEM images, electrochemical performance curves) is available in the online version of this article at https://doi.org/10.1007/s12274-020-3225-7.

References

[1] Patel, P. Improving the lithium-ion battery. *ACS Cent. Sci.* **2015**, *1*, 161–162.

[2] Bresser, D.; Hosoi, K.; Howell, D.; Li, H.; Zeisel, H.; Amine, K.; Passerini, S. Perspectives of automotive battery R&D in China, Germany, Japan, and the USA. *J. Power Sources* **2018**, *382*, 176–178.

[3] Zhao, W. G.; Zheng, J. M.; Zou, L. F.; Jia, H. P.; Liu, B.; Wang, H.; Engelhard, M. H.; Wang, C. M.; Xu, W.; Yang, Y. et al. High voltage operation of Ni-rich NMC cathodes enabled by stable electrode/electrolyte interphases. *Adv. Energy Mater.* **2018**, *8*, 1800297.

[4] Li, W. D.; Lee, S.; Manthiram, A. High-nickel NMA: A cobalt-free alternative to NMC and NCA cathodes for lithium-ion batteries. *Adv. Mater.* **2020**, *32*, 2002718.

[5] Li, Y. Z.; Yan, K.; Lee, H. W.; Lu, Z. D.; Liu, N.; Cui, Y. Growth of conformal graphene cages on micrometre-sized silicon particles as stable battery anodes. *Nat. Energy* **2016**, *1*, 15029.

[6] Tao, W.; Wang, P.; You, Y.; Park, K.; Wang, C. Y.; Li, Y. K.; Cao, F. F.; Xin, S. Strategies for improving the storage performance of silicon-based anodes in lithium-ion batteries. *Nano Res.* **2019**, *12*, 1739–1749.

[7] Wang, B.; Ryu, J.; Choi, S.; Zhang, X. H.; Pribat, D.; Li, X. L.; Zhi, L. J.; Park, S.; Ruoff, R. S. Ultrafast-charging silicon-based coral-like network anodes for lithium-ion batteries with high energy and power densities. *ACS Nano* **2019**, *13*, 2307–2315.

[8] Zhu, K. L.; Li, Q.; Xue, Z. M.; Yu, Q.; Liu, X. C.; Shan, Z. Q.; Liu, K. Mesoporous TiO_2 spheres as advanced anodes for low-cost, safe, and high-areal-capacity lithium-ion full batteries. *ACS Appl. Nano Mater.* **2020**, *3*, 1019–1027.

[9] Li, N.; Zhou, G. M.; Fang, R. P.; Li, F.; Cheng, H. M. TiO_2/graphene sandwich paper as an anisotropic electrode for high rate lithium ion batteries. *Nanoscale* **2013**, *5*, 7780–7784.

[10] Wang, D. H.; Choi, D.; Li, J.; Yang, Z. G.; Nie, Z. M.; Kou, R.; Hu, D. H.; Wang, C. M.; Saraf, L. V.; Zhang, J. G. et al. Self-assembled TiO_2–graphene hybrid nanostructures for enhanced Li-ion insertion. *ACS Nano* **2009**, *3*, 907–914.

[11] Hwang, C. H.; Kim, H. E.; Nam, I.; Bang, J. H. Polygonal multi-polymorphed $Li_4Ti_5O_{12}$@rutile TiO_2 as anodes in lithium-ion batteries. *Nano Res.* **2019**, *12*, 897–904.

[12] Wang, Q.; Shen, L.; Xue, T.; Cheng, G.; Huang, C. Z.; Fan, H. J.; Feng, Y. P. Single-crystalline TiO_2(B) nanobelts with unusual large exposed {100} facets and enhanced Li-storage capacity. *Adv. Funct. Mater.* **2020**, 2002187.

[13] Li, W.; Wang, F.; Feng, S. S.; Wang, J. X.; Sun, Z. K.; Li, B.; Li, Y. H.; Yang, J. P.; Elzatahry, A. A.; Xia, Y. Y. et al. Sol–gel design strategy for ultradispersed TiO_2 nanoparticles on graphene for high-performance lithium ion batteries. *J. Am. Chem. Soc.* **2013**, *135*, 18300–18303.

[14] Qiu, B. C.; Xing, M. Y.; Zhang, J. L. Mesoporous TiO_2 nanocrystals grown *in situ* on graphene aerogels for high photocatalysis and lithium-ion batteries. *J. Am. Chem. Soc.* **2014**, *136*, 5852–5855.

[15] Li, W.; Wang, F.; Liu, Y. P.; Wang, J. X.; Yang, J. P.; Zhang, L. J.; Elzatahry, A. A.; Al-Dahyan, D.; Xia, Y. Y.; Zhao, D. General strategy to synthesize uniform mesoporous TiO_2/graphene/mesoporous TiO_2 sandwich-like nanosheets for highly reversible lithium storage. *Nano Lett.* **2015**, *15*, 2186–2193.

[16] Liu, H.; Li, W.; Shen, D. K.; Zhao, D. Y.; Wang, G. X. Graphitic carbon conformal coating of mesoporous TiO_2 hollow spheres for high-performance lithium ion battery anodes. *J. Am. Chem. Soc.* **2015**, *137*, 13161–13166.

[17] Zhu, K. L.; Liu, X. Y.; Du, J. Y.; Tian, J. H.; Wang, Y.; Liu, S. Z.; Shan, Z. Q. *In situ* synthesis of mesoporous single-grain layer anatase TiO_2 nanosheets without additives via a mild and simple process for a long-term Li-ion battery. *J. Mater. Chem. A* **2015**, *3*, 6455–6463.

[18] Guan, B. Y.; Yu, L.; Li, J.; Lou, X. W. D. A universal cooperative assembly-directed method for coating of mesoporous TiO_2 nanoshells with enhanced lithium storage properties. *Sci. Adv.* **2016**, *2*, e1501554.

[19] Zhu, K. L.; Sun, Y. H.; Wang, R. M.; Shan, Z. Q.; Liu, K. Fast synthesis of uniform mesoporous titania submicrospheres with high tap densities for high-volumetric performance Li-ion batteries. *Sci. China Mater.* **2017**, *60*, 304–314.

[20] Yu, W. B.; Hu, Z. Y.; Jin, J.; Yi, M.; Yan, M.; Li, Y.; Wang, H. E.; Gao, H. X.; Mai, L. Q.; Hasan, T. et al. Unprecedented and highly stable lithium storage capacity of (001) faceted nanosheet-constructed hierarchically porous TiO_2/rGO hybrid architecture for high-performance Li-ion batteries. *Natl. Sci. Rev.* **2020**, *7*, 1046–1058.

[21] Lee, D. H.; Lee, B. H.; Sinha, A. K.; Park, J. H.; Kim, M. S.; Park, J.; Shin, H.; Lee, K. S.; Sung, Y. E.; Hyeon, T. Engineering titanium dioxide nanostructures for enhanced lithium-ion storage. *J. Am. Chem. Soc.* **2018**, *140*, 16676–16684.

[22] Wang, B. Y.; Yuan, W.; Zhang, X. M.; Xiang, M. W.; Zhang, Y.; Liu, H.; Wu, H. Sandwiching defect-Rich $TiO_{2-\delta}$ nanocrystals into a three-dimensional flexible conformal carbon hybrid matrix for long-cycling and high-rate Li/Na-ion batteries. *Inorg. Chem.* **2019**, *58*, 8841–8853.

[23] Modarres, M. H.; Engelke, S.; Jo, C.; Seveno, D.; De Volder, M. Self-assembly of hybrid nanorods for enhanced volumetric performance of nanoparticles in Li-ion batteries. *Nano Lett.* **2019**, *19*, 228–234.

[24] Shin, J. Y.; Samuelis, D.; Maier, J. Sustained lithium-storage performance of hierarchical, nanoporous anatase TiO_2 at high rates: Emphasis on interfacial storage phenomena. *Adv. Funct. Mater.* **2011**, *21*, 3464–3472.

[25] Liu, S. H.; Wang, Z. Y.; Yu, C.; Wu, H. B.; Wang, G.; Dong, Q.; Qiu, J. S.; Eychmüller, A.; Lou, X. W. A flexible TiO_2(B)-based battery electrode with superior power rate and ultralong cycle life. *Adv. Mater.* **2013**, *25*, 3462–3467.

[26] He, L. F.; Wang, C. D.; Yao, X. L.; Ma, R. G.; Wang, H. K.; Chen, P. R.; Zhang, K. Synthesis of carbon nanotube/mesoporous TiO_2 coaxial nanocables with enhanced lithium ion battery performance. *Carbon* **2014**, *75*, 345–352.

[27] Wang, D. D.; Shan, Z. Q.; Na, R.; Huang, W. L.; Tian, J. H. Solvothermal synthesis of hedgehog-like mesoporous rutile TiO_2 with improved lithium storage properties. *J. Power Sources* **2017**, *337*, 11–17.

[28] Zhang, G. Q.; Wu, H. B.; Song, T.; Paik, U.; Lou, X. W. TiO_2 hollow spheres composed of highly crystalline nanocrystals exhibit superior lithium storage properties. *Angew. Chem., Int. Ed.* **2014**, *53*, 12590–12593.

[29] Zhu, K. L.; Luo, Y. F.; Zhao, F.; Hou, J. W.; Wang, X. W.; Ma, H.; Wu, H.; Zhang, Y. G.; Jiang, K. L.; Fan, S. S. et al. Free-standing, binder-free titania/super-aligned carbon nanotube anodes for flexible and fast-charging Li-ion batteries. *ACS Sustainable Chem. Eng.* **2018**, *6*, 3426–3433.

[30] Zhang, L. H.; Qin, X. Y.; Zhao, S. Q.; Wang, A.; Luo, J.; Wang, Z. L.; Kang, F. Y.; Lin, Z. Q.; Li, B. H. Advanced matrixes for binder-free nanostructured electrodes in lithium-ion batteries. *Adv. Mater.* **2020**, *32*, 1908445.

[31] Liu, K.; Sun, Y. H.; Chen, L.; Feng, C.; Feng, X. F.; Jiang, K. L.; Zhao, Y. G.; Fan, S. S. Controlled growth of super-aligned carbon nanotube arrays for spinning continuous unidirectional sheets with tunable physical properties. *Nano Lett.* **2008**, *8*, 700–705.

[32] Jiang, K. L.; Wang, J. P.; Li, Q. L.; Liu, L.; Liu, C. H.; Fan, S. S. Superaligned carbon nanotube arrays, films, and yarns: A road to applications. *Adv. Mater.* **2011**, *23*, 1154–1161.

[33] Sun, L.; Wang, D. T.; Luo, Y. F.; Wang, K.; Kong, W. B.; Wu, Y.; Zhang, L. N.; Jiang, K. L.; Li, Q. Q.; Zhang, Y. H. et al. Sulfur embedded in a mesoporous carbon nanotube network as a binder-free electrode for high-performance lithium–sulfur batteries. *ACS Nano* **2016**, *10*, 1300–1308.

[34] Zhang, Y.; Franklin, N. W.; Chen, R. J.; Dai, H. Metal coating on suspended carbon nanotubes and its implication to metal-tube interaction. *Chem. Phys. Lett.* **2000**, *331*, 35–41.

[35] Yang, H. G.; Sun, C. H.; Qiao, S. Z.; Zou, J.; Liu, G.; Smith, S. C.; Cheng, H. M.; Lu, G. Q. Anatase TiO_2 single crystals with a large percentage of reactive facets. *Nature* **2008**, *453*, 638–641.

[36] Iijima, S. Helical microtubules of graphitic carbon. *Nature* **1991**, *354*, 56–58.

[37] Huang, F. M.; Yue, K. T.; Tan, P. H.; Zhang, S. L.; Shi, Z.; Zhou, X.; Gu, Z. Temperature dependence of the Raman spectra of carbon nanotubes. *J. Appl. Phys.* **1998**, *84*, 4022–4024.

[38] Alhomoudi, I. A.; Newaz, G. Residual stresses and Raman shift relation in anatase TiO_2 thin film. *Thin Solid Films* **2009**, *517*, 4372–4378.

[39] Zhu, K. L.; Tian, J. H.; Liu, Y. P.; Lin, N.; Tang, Q. W.; Yu, X. M.; Zhu, Y. M.; Shan, Z. Q. Submicron-sized mesoporous anatase TiO_2 beads with a high specific surface synthesized by controlling reaction conditions for high-performance Li-batteries. *RSC Adv.* **2013**, *3*, 13149–13155.

[40] Xing, Y. L.; Wang, S. B.; Fang, B. Z.; Song, G.; Wilkinson, D. P.; Zhang, S. C. N-doped hollow urchin-like anatase TiO_2@C composite as a novel anode for Li-ion batteries. *J. Power Sources* **2018**, *385*, 10–17.

[41] Zhang, C.; Liu, S. T.; Qi, Y. C.; Cui, F. M.; Yang, X. J. Conformal carbon coated TiO_2 aerogel as superior anode for lithium-ion batteries. *Chem. Eng. J.* **2018**, *351*, 825–831.

[42] Yang, S. B.; Feng, X. L.; Müllen, K. Sandwich-like, graphene-based titania nanosheets with high surface area for fast lithium storage. *Adv. Mater.* **2011**, *23*, 3575–3579.

[43] Gao, M.; Bao, Y. B.; Qian, Y. X.; Deng, Y. F.; Li, Y. W.; Chen, G. H. Porous anatase-TiO_2(B) dual-phase nanorods prepared from *in situ* pyrolysis of a single molecule precursor offer high performance lithium-ion storage. *Inorg. Chem.* **2018**, *57*, 12245–12254.

[44] Luo, M.; Yu, X.; Zhao, W. X.; Xu, R. M.; Liu, Y.; Shen, H. Polymer-promoted synthesis of porous TiO_2 nanofibers decorated with N-doped carbon by mechanical stirring for high-performance Li-ion storage. *ACS Appl. Mater. Interfaces* **2018**, *10*, 35060–35068.

[45] Zhou, T. F.; Zheng, Y.; Gao, H.; Min, S. D.; Li, S.; Liu, H. K.; Guo, Z. P. Surface engineering and design strategy for surface-amorphized TiO_2@graphene hybrids for high power Li-ion battery electrodes. *Adv. Sci.* **2015**, *2*, 1500027.

[46] Petkovich, N. D.; Rudisill, S. G.; Wilson, B. E.; Mukherjee, A.; Stein, A. Control of TiO_2 grain size and positioning in three-dimensionally ordered macroporous TiO_2/C composite anodes for lithium ion batteries. *Inorg. Chem.* **2014**, *53*, 1100–1112.

[47] Jo, M. S.; Park, G. D.; Kang, Y. C.; Cho, J. S. Design and synthesis of interconnected hierarchically porous anatase titanium dioxide nanofibers as high-rate and long-cycle-life anodes for lithium-ion batteries. *Nanoscale* **2018**, *10*, 13539–13547.

[48] Wagemaker, M.; Borghols, W. J. H.; Mulder, F. M. Large impact of particle size on insertion reactions. A case for anatase Li_xTiO_2. *J. Am. Chem. Soc.* **2007**, *129*, 4323–4327.

[49] Borghols, W. J. H.; Lützenkirchen-Hecht, D.; Haake, U.; Van Eck, E. R. H.; Mulder, F. M.; Wagemaker, M. The electronic structure and ionic diffusion of nanoscale $LiTiO_2$ anatase. *Phys. Chem. Chem. Phys.* **2009**, *11*, 5742–5748.

[50] Wu, H. B.; Chen, J. S.; Hng, H. H.; Lou, X. W. D. Nanostructured metal oxide-based materials as advanced anodes for lithium-ion batteries. *Nanoscale* **2012**, *4*, 2526–2542.

[51] Wang, S. B.; Guan, B. Y.; Yu, L.; Lou, X. W. Rational design of three-layered TiO_2@Carbon@MoS_2 hierarchical nanotubes for enhanced lithium storage. *Adv. Mater.* **2017**, *29*, 1702724.

[52] Fang, Y. Z.; Hu, R.; Liu, B. Y.; Zhang, Y. Y.; Zhu, K.; Yan, J.; Ye, K.; Cheng, K.; Wang, G. L.; Cao, D. X. MXene-derived TiO_2/reduced graphene oxide composite with an enhanced capacitive capacity for Li-ion and K-ion batteries. *J. Mater. Chem. A* **2019**, *7*, 5363–5372.

[53] Deng, C. J.; Lau, M. L.; Ma, C. R.; Skinner, P.; Liu, Y. Z.; Xu, W. Q.; Zhou, H.; Zhang, X. H.; Wu, D.; Yin, Y. D. et al. A mechanistic study of mesoporous TiO_2 nanoparticle negative electrode materials with varying crystallinity for lithium ion batteries. *J. Mater. Chem. A* **2020**, *8*, 3333–3343.

[54] Choi, S.; Kwon, T. W.; Coskun, A.; Choi, J. W. Highly elastic binders integrating polyrotaxanes for silicon microparticle anodes in lithium ion batteries. *Science* **2017**, *357*, 279–283.